PNAS RESEARCH ARTICLE | ENVIRONMENTAL SCIENCES OPEN ACCESS

Understanding the mechanisms of anisotropic dissolution in metal oxides by applying radiolysis simulations to liquid-phase TEM

Lili Liu[a,1], Michel Sassi[a,1], Xin Zhang[a,2], Elias Nakouzi[a], Libor Kovarik[a], Sichuang Xue[a], Biao Jin[a], Kevin M. Rosso[a,2], and James J. De Yoreo[a,b,2]

Edited by Galen Stucky, University of California Santa Barbara, Santa Barbara, CA; received January 20, 2021; accepted April 4, 2023

Iron-based redox-active minerals are ubiquitous in soils, sediments, and aquatic systems. Their dissolution is of great importance for microbial impacts on carbon cycling and the biogeochemistry of the lithosphere and hydrosphere. Despite its widespread significance and extensive prior study, the atomic-to-nanoscale mechanisms of dissolution remain poorly understood, particularly the interplay between acidic and reductive processes. Here, we use in situ liquid-phase-transmission electron microscopy (LP-TEM) and simulations of radiolysis to probe and control acidic versus reductive dissolution of akaganeite (β–FeOOH) nanorods. Informed by crystal structure and surface chemistry, the balance between acidic dissolution at rod tips and reductive dissolution at rod sides was systematically varied using pH buffers, background chloride anions, and electron beam dose. We find that buffers, such as bis-tris, effectively inhibited dissolution by consuming radiolytic acidic and reducing species such as superoxides and aqueous electrons. In contrast, chloride anions simultaneously suppressed dissolution at rod tips by stabilizing structural elements while promoting dissolution at rod sides through surface complexation. Dissolution behaviors were systematically varied by shifting the balance between acidic and reductive attacks. The findings show LP-TEM combined with simulations of radiolysis effects can provide a unique and versatile platform for quantitatively investigating dissolution mechanisms, with implications for understanding metal cycling in natural environments and the development of tailored nanomaterials.

akaganeite | dissolution | liquid cell TEM

Significance

Dissolution of redox-active metal oxides plays a fundamental role in the environment and technological applications. However, dissolution mechanisms remain poorly understood at nanoscale, particularly the interplay between acidic and reductive processes. Using akaganeite (β–FeOOH) nanorods in liquid-phase-transmission electron microscopy, combined with deterministic simulations of dose rate–dependent radiolytic speciation, we exploit a quantitative connection between observed dissolution rate and behavior to modeled solution speciation at steady state to delineate underlying mechanisms. Gaining quantitative control of the balance between acidic and reductive dissolution, which can be varied by using pH buffers, chloride anions, and electron beam dose, enabled us to understand and tune resulting dissolution behaviors. The findings provide insights into processes controlling the dissolution of minerals in natural environments.

Iron is the most abundant redox-active element in the earth's crust and its global biogeochemical cycling is coupled to a variety of processes in the hydrosphere and lithosphere (1–5). Iron (III) oxyhydroxide nanoparticles (NPs), of widespread occurrence in soils and rocks, are particularly important both in the environment and in technological applications, partly because they are acid soluble and readily reduced and thus can be transformed into more labile forms of iron or transformed into other phases (2, 6–10). For instance, in soils, sediments, and aquatic systems, the conversion of iron oxyhydroxide NPs into much more soluble ferrous iron through reductive dissolution is critical to iron bioavailability (11, 12). Consequently, extensive research has been performed to understand dissolution mechanisms for these NPs, which tend to be categorized as acidic (1, 13, 14), reductive (15–18), acidic/reductive (14, 19), and ligand assisted (20). However, despite the interconnections between some of these pathways at a fundamental level, complications arising from diverse structure types, different reactivities of specific facets and crystal morphologies, and the critical role of variable defect content have hindered the development of a detailed, predictive understanding.

Phenomenological trends in iron (III) oxyhydroxide dissolution kinetics have been established using macroscopic batch experiments. For example, reductive dissolution is generally faster than nonreductive dissolution (e.g., proton-promoted or ligand-assisted dissolution) (21). This has been attributed to a higher lability of Fe^{2+}–O versus Fe^{3+}–O bonds and thereby faster iron site destabilization and release. However, both the reduction potential and stability of reduced iron at various NP surfaces are site specific, with the nature of the sites dependent on the structure of exposed facets (22, 23). Similarly, for proton-promoted or ligand-assisted dissolution, the reactivity depends on facet-specific exposure of oxo and hydroxo functional groups coordinating to surface iron sites. That the dissolution behavior should be controlled by facet-specific local structure was recently illustrated in an ab initio modeling study by Klyukin et al. (2), who showed that activation energies for acidic versus reductive release of iron differ primarily in the initial bond breaking events. Despite these generalities, it remains difficult to predict a priori which crystal facets of NPs might preferentially dissolve by, for instance, acidic versus reductive attack.

Akageneite (β–FeOOH) represents a typical natural mineral of iron oxyhydroxide and appears as a precursor to the formation of goethite (α–FeOOH), hematite (α–Fe_2O_3), and magnetite (Fe_3O_4) (5). Given that most replacement reactions occur through dissolution

The authors declare no competing interest.

This article is a PNAS Direct Submission.

[1]L.L. and M.S. contributed equally to this work.

[2]To whom correspondence may be addressed. Email: xin.zhang@pnnl.gov, kevin.rosso@pnnl.gov, or james.deyoreo@pnnl.gov.

This article contains supporting information online at https://www.pnas.org/lookup/suppl/doi:10.1073/pnas.2101243120/-/DCSupplemental.

Published May 30, 2023.

of the precursor phase as the replacement mineral nucleates and grows, the mechanism of akageneite dissolution is important, not just for understanding the dissolution of iron-based redox-active minerals, but for understanding their growth as well. Moreover, in contrast to goethite and hematite, the dissolution degree and rate of akageneite is much higher (24), which in turn allows us to observe the dissolution process at the nanoscale on a short time scale. To understand which dissolution mechanism is at work, taking akageneite nanorods as a model system, we used in situ liquid-phase-transmission electron microscopy (LP-TEM) to investigate the dissolution dynamics. Beyond being highly spatially resolved, the LP-TEM approach is perhaps unique in its ability to span acidic versus reductive dissolution regimes by manipulating the solution chemistry through standard wet chemistry combined with the effect of beam-induced changes in speciation. Beam-induced radiolysis of the aqueous solution produces reactive solution species, such as superoxides and aqueous electrons and protons (25–27). As recently demonstrated by Schneider et al. (28), the dose rate–dependent acidity and speciation and lifetimes of the various reducing and oxidizing radicals can be modeled, including e_{aq}^-, H•, H_2, H_3O^+, OH^-, H_2O_2, OH•, and O_2, which are known to play a role in enhancing dissolution (28–30). Thus by adjusting the buffering capacity of the initial solution through standard wet chemistry, the pH and concentrations of redox-active species at steady state are determined by the selected e-beam dose rate. By combining LP-TEM results with simulations, we addressed the following questions: 1) What are the main factors controlling the dissolution in acidic solutions and what are the beam effects? 2) Is there a facet-dependent behavior to the dissolution and to what extent does this depend on acidic versus reductive mechanisms? 3) What is the role of crystal defects in dissolution? In addition to being able identify major mechanisms controlling the facet-specific dissolution behavior and how these connect to overall dissolution rates, by studying the effects of pH buffers and chloride (Cl^-) ions on dissolution, we were also able to identify regimes of irradiation and buffer concentration in which the nanorods are stable against beam-induced dissolution.

Results and Discussion

Akaganeite Acidic Dissolution and the Effect of Electron Beam Irradiation. Within the Fe(III)-(oxyhydr)oxide family, the akaganeite crystal structure is distinguished by the bcc packing of the anion lattice, compared to the more common hcp packing found in goethite (α–FeOOH) and hematite (α–Fe_2O_3). However, similar to goethite, the framework is based on double chains of edge-sharing $Fe(O,OH)_6$ octahedra that propagate along the [010] direction interconnected by corner-sharing oxo bridges (Fig. 1 *A* and *B*). This is the basis for the preferential rod-like crystallite habit of both goethite and akageneite. The principal topological difference between the two structures is as follows: While in goethite, the double-chains form 1 × 2 channels, in akaganeite, the double-chains form more open 2 × 2 channels, which are stabilized by incorporation of anionic species, typically chloride or bromide (13). In addition to being structurally related, akaganeite is also compositionally

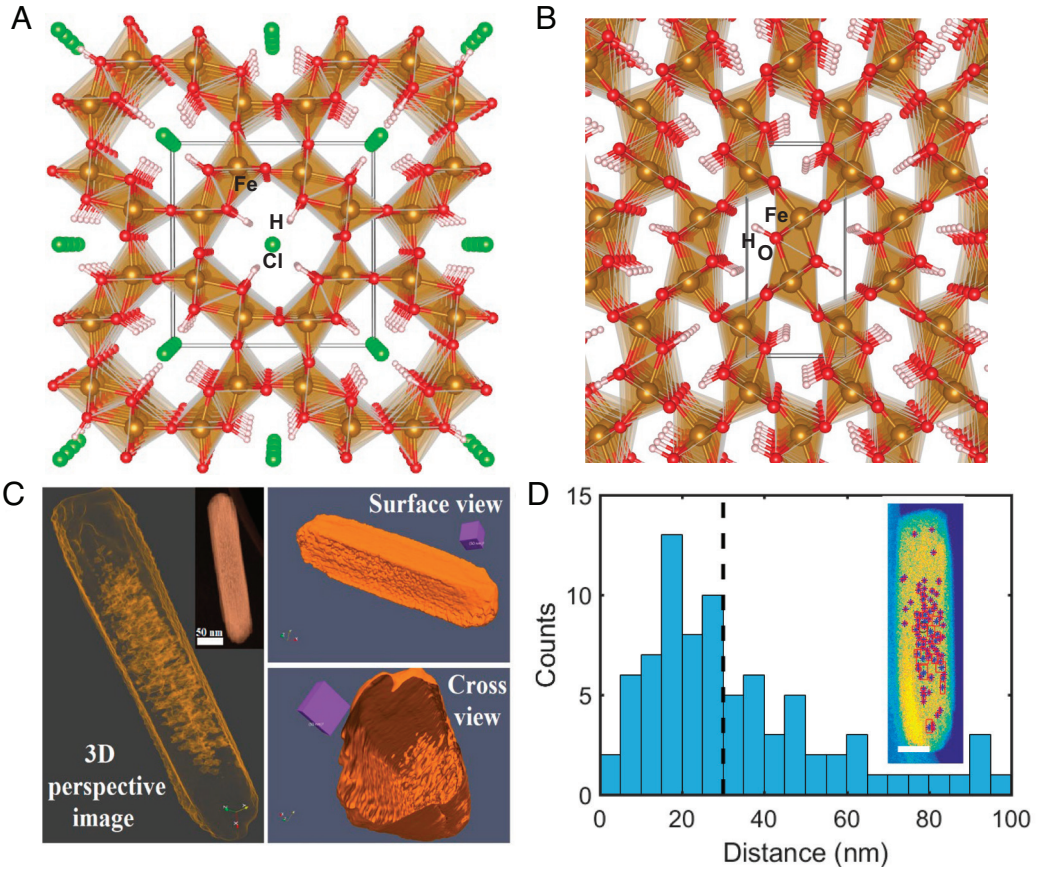

Fig. 1. Structural models featuring the topological similarity between (*A*) akageneite, and (*B*) goethite. The orange balls represent Fe atoms, red balls are oxygen atoms, light pink balls are hydrogen atoms, and green balls are chlorine atoms. (*C*) 3D STEM-HAADF tomographic reconstruction and cross-section of akaganeite nanorod to show the pore defect distribution (*Left* is a perspective image and the *Inset* is the STEM image, right-top is the surface view and right-bottom is the cross-sectional view along the [010] direction). (*D*) Pore distribution counts versus the distance (in nm) from the center of the nanorod determined from automated image analysis; the scale bar in the *Inset* is 30 nm.

similar to goethite, differing only by the 2 to 6 wt% chloride or bromide ions residing within the channels (31). It is, in fact, principally the presence of chloride or bromide that tends to favor akageneite formation over goethite at low pH.

We used a hydrothermal method to synthesize akaganeite nanorods elongated along the [010] direction and measuring, on average, ~250 nm in length and ~50 nm in width (See *Methods* for details). In addition to standard characterization of material crystallinity and purity (*SI Appendix*, Fig. S1*A*), we used high-angle annular dark-field-scanning transmission electron microscopy (HAADF-STEM, Movies S1 and S2) with 3D tomography to carefully scrutinize our nanorods for defect content, an important potential contributor to the dissolution rate and morphological evolution. The imaging clearly revealed a prominent nanoporosity within the central portions of the nanorods (Fig. 1*C*). Statistical analysis of pore concentration versus distance from the center of the nanorods is given in Fig. 1*D*, which shows that the dominant location of the pores is within 30 nm of the nanorod center (dashed black line as the boundary). The reason why more defects form near the center of the nanorods is unclear, but we speculate that could arise from initially higher growth rates at the early stage of nanorod precipitation (32, 33).

The chemical composition of akaganeite nanorods was analyzed by STEM-EDS mapping and XPS, as shown in *SI Appendix*, Fig. S1 *E–G*. The STEM-EDS mapping indicated that the ratio of Fe to Cl is around 6.4:1, but the XPS wide-scan photoemission spectrum demonstrated that the ratio of Fe to Cl is around 9.2:1. The XPS can only detect the surface elements with a depth of around 1 to 2 nm. Thus, it is reasonable to hypothesize that the Cl concentration inside of the akaganeite nanorods is higher than that of outside. The linear EDS scanning also confirms that the Cl concentration on the sides of the akaganeite nanorods is lower than that in the center (*SI Appendix*, Fig. S2). Based on 3D tomography described above, the defect density in the center of the akaganeite nanorods is much higher than that on the sides. Thus, the Cl concentration in the areas with defects may be higher than that in the defect-free areas, a conclusion that is further supported by the EDS point scanning (*SI Appendix*, Fig. S3). These results suggest that the defects in the akaganeite nanorods may trap more Cl than the normal 2 × 2 channel structures. Notwithstanding, foreknowledge of this defect content and its chemical composition was essential for informing interpretations of nanorod dissolution behavior in ensuing dissolution experiments.

Using these akageneite nanorods, two sets of experiments were carried out to determine the role of acidity on the dissolution behavior (Fig. 2). The first was performed ex situ in the absence of e-beam irradiation in strongly acidic conditions (0.5 mol/L HCl) at 80 °C, yielding nominally pH 0.3 solution. As shown in Fig. 2*A*, in this case, the tapered ends of the nanorods became squared to produce flat [010] facets, and this morphology was maintained as the rods progressively shortened as dissolution continued. However, the width of the nanorods remained largely unchanged during the reaction, indicating that acidic dissolution selectively favors iron release along the [010] direction defined by the tunnel structure (*SI Appendix*, Fig. S1*B*). This finding agrees well with previous understanding (13) that, in acidic conditions, Fe(III) release occurs primarily at (010) nanorod tip surfaces rather than from the prismatic [100] and [001] surfaces. This arises, at least in part, because exposed at rod tip surfaces is a high density of acid-reactive hydroxo functional groups coordinating the truncated ends of the double chains, which lowers the activation energy for acidic release of ferric iron relative to the less reactive hydroxo and oxo functional groups exposed along the sides of the double chains (2). Furthermore, at the nanorod tips, protons can penetrate into the tunnels and assist in the removal of Cl^- ions (13). The combined effect of acid attack at double-chain terminated faces in concert with release of Cl^- from tunnels destabilizes the akaganeite framework at rod tips, leading to rapid acidic dissolution along the [010] direction. The akaganeite dissolution process in acid via the classical protonation mechanism is illustrated in *SI Appendix*, Fig. S4.

The second set of experiments was conducted using in situ LP-TEM in pure water under e-beam irradiation (Fig. 2*B*) for comparison with the behavior observed under unirradiated acidic conditions. Pure water (~pH 7) was selected in anticipation that equilibration with 5 mM akageneite in air increases the initial acidity to around 5.05, which during e-beam irradiation would be acidified further by radiolytic speciation involving transient H_3O^+ (~pH 4) (28). Given the observed dissolution behavior in acidic conditions, we hypothesize that under the e-beam, the total acidity would likewise induce dissolution along the [010] direction. Indeed, as expected, beam-induced dissolution of the akaganeite nanorods occurred along the [010] direction. However, in striking contrast, dissolution was much faster and now also observed along the prismatic sides of the nanorods, i.e., along the [001]/[100] directions. Although the initial solution was much less acidic than that in the *ex situ* experiments, in this case, the overall dissolution occurred in seconds rather than hundreds of minutes. We note that recrystallization could occur and might then also play a role in controlling the anisotropic morphology of akaganeite during the dissolution process, especially in Fe(II)-catalyzed environments (e-beam irradiation conditions) (3, 5, 33). However, in this work, we only observed the dissolution of akageneite nanorods in both ex situ and in situ experiments. There is no evidence from our direct imaging or structural analyses to support the occurrence of recrystallization on our experimental time scale. Previous studies of Fe(II)-catalyzed recrystallized iron oxide nanoparticles have demonstrated that the time scale to obtain an obvious morphology changes is several days at room temperature (3, 34, 35) and several hours at 75 °C (36).

Note that in both experiments, despite the availability of nanopore defects near the center of the rods, which could serve as preferential etching sites, the TEM data show that the facet direction exerts the prevailing control over dissolution in these cases. To quantify these direction-specific kinetics, we used a geometric contraction model. In this model, the reaction is controlled by the reaction interface progressing toward the center, assuming that the reaction occurs only on the surface (37). For simplicity, we regard the nanorods to be cylindrical particles for which the dissolution rate in any direction is assumed to be a constant. That is, $X = X_0 (1 - Kt)$, where X is the dimension of the particle in a given direction, X_0 is the initial value of that dimension, K is the rate constant, and t is the time. Thus, defining the function $\alpha = 1 - L/L_{Fe,0}$ or $1 - W/W_{Fe,0}$, we quantified the rate constants K_L and K_W for dissolution along the nanorod length and width, respectively, by plotting α versus t (Fig. 2 *C* and *D*). For acidic dissolution–absent irradiation, the rate constant K_L for dissolution along the nanorod tips ([010]) was found to exceed K_W for dissolution along the nanorod width ([001]/[100]) by more than a factor of 250 (Fig. 2*C*). In contrast, under beam-induced radiolytic speciation, the two dissolution rate constants are similar, within a factor of 2 (Fig. 2*D*). Finally, this linear model allowed us to quantify the differences in the overall dissolution kinetics observed. In the case of acidic dissolution, the rates were 0.007 s^{-1} (length) and 2.8 × 10^{-5} s^{-1} (width), while under e-beam irradiation, the rates were 0.05 s^{-1} (length) and 0.03 s^{-1} (width).

Clearly, a key difference in these two experiments is the solution speciation beyond acidity alone. In particular, e-beam irradiation

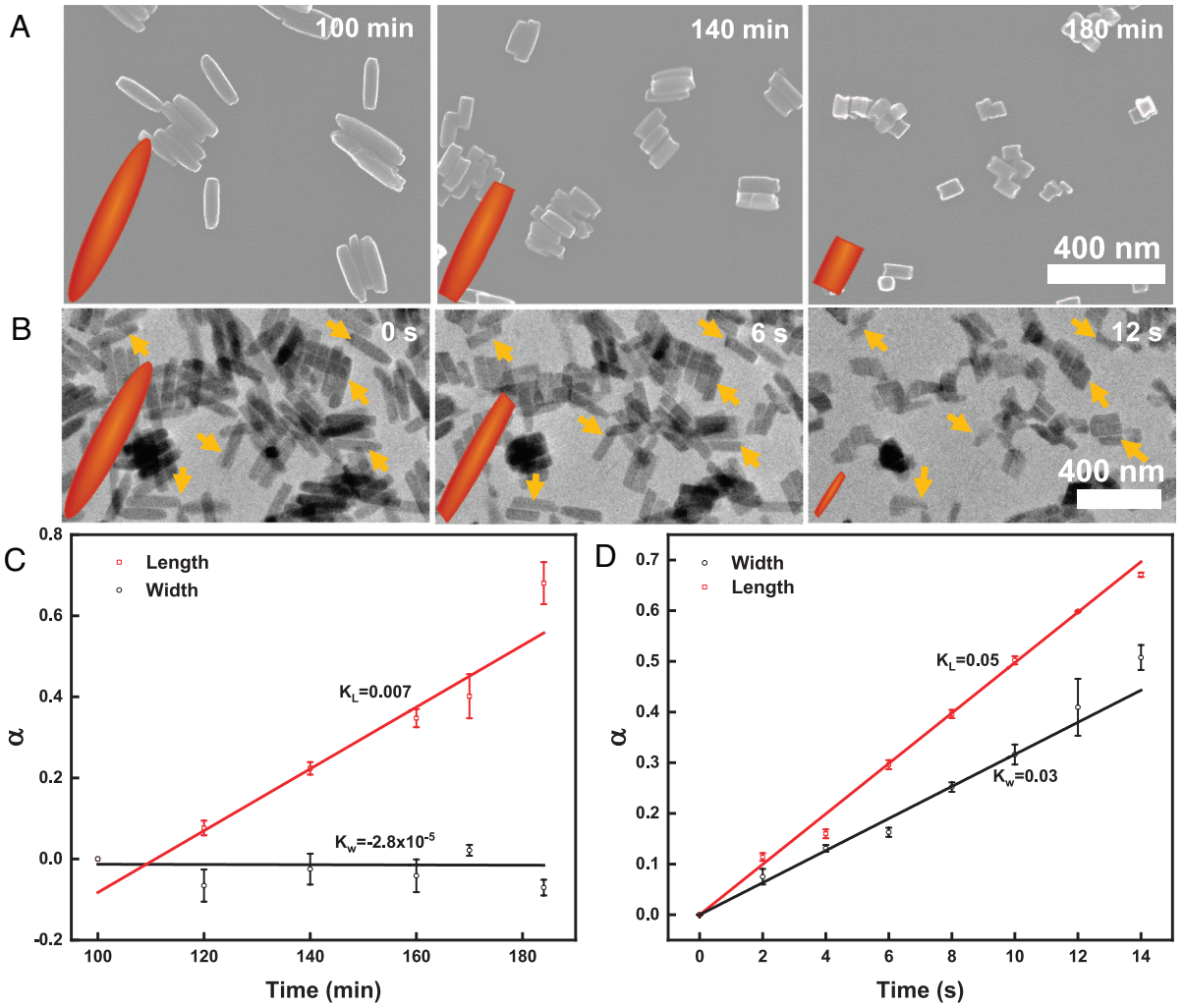

Fig. 2. (*A*) Ex situ SEM images showing the time-dependent acidic dissolution behavior of akaganeite (5 mM) in the presence of 0.5 M HCl, without e-beam exposure. (*B*) Time evolution of akaganeite (5 mM) dissolution as observed by LP-TEM at an e-beam dose rate of 0.53 e/Å^{2}s. (*C* and *D*) Dissolution rates from panels *A* and *B*, respectively, along the length (L) and width (W) plotted as α versus time (see text for details). K, obtained from the linear data fitting, is the dissolution rate constant, expressed in min^{-1} in *C* and s^{-1} in *D*. Note: For both ex situ and in situ experiments, we measured the length and width of more than 25 nanorods at each time point and then plotted the average value with error bars equal to one SD.

also produces numerous reducing and oxidizing radicals in water, including hydrated electrons (e_{aq}^-), H•, H_2, H_3O^+, OH^-, H_2O_2, OH•, and O_2 (28, 29). As the overall dissolution rate is much faster with beam-induced radiolysis, despite being less acidic, it is reasonable to hypothesize that the dissolution rate is enhanced by reductive radical species such as e(aq)-, H•, and OH•. Previous experimental work and simulations revealled that Fe(III) reduction to Fe(II) can lead to more rapid Fe release from iron (oxyhydr) oxide surfaces than the acidic mechanism alone (2, 18, 21). These radical species should be capable of reducing Fe(III) to Fe(II) at nanorod surfaces (35, 36) and driving the system to lower redox potentials (38, 39). Our principal evidence that reductive dissolution is occurring in this case is the greatly accelerated overall dissolution rate that includes dissolution along the [001]/[100] directions.

Analysis of Radiolysis Products and Their Impact on Dissolution Rates. To explore the potential for radiolytic species to play a role in akaganeite dissolution, we developed an akaganeite/water beam–induced reactive interface model and performed deterministic simulations to quantify the contributions of protonation, reduction, and radiolytic species to the dissolution rate (*SI Appendix*, *Kinetic Model* and Fig. 3) (40). Fig. 3*A* compares the predictions of the simulations to the observed dissolution rate for similar initial conditions [5 mM akaganeite in pure water (pH = 7) under exposure to the e-beam at the dose rate used in the TEM experiments]. In agreement with previous studies (28), the simulations found that e-beam irradiation reduces the pH of the solution substantially, in this case to 4.27 for the dose rate of 0.53 e/Å^{2}s (4.24 × 10^8 Gy/s). At this lower pH, Fig. 3*A* shows that the dissolution induced by acidity alone is not fast enough to achieve complete dissolution within 100 s. In particular, we note that at pH = 4.27, proton-promoted dissolution is slower than that observed in the ex situ SEM experiments at pH = 0.3.

As aqueous electrons (e_{aq}^-) are produced during water radiolysis, using our deterministic simulations, we quantified their contribution to akaganeite dissolution by reduction and found it to be an order of magnitude greater than that due to proton-promoted dissolution. However, the time needed for dissolution is still predicted to be longer than 10^4 s. Consequently, we evaluated the effect of other transient species generated during water radiolysis, including HO_2, HO_2^-, H_2O_2, and O_2^-. While HO_2, HO_2^-, and H_2O_2 do not have noticeable impacts on the akaganeite dissolution rate, we found that O_2^-, and, more specifically, the transfer of electrons from O_2^- to surface Fe(III) to produce Fe(II) and O_2 (Re109 in *SI Appendix*, Table S4) make an important contribution

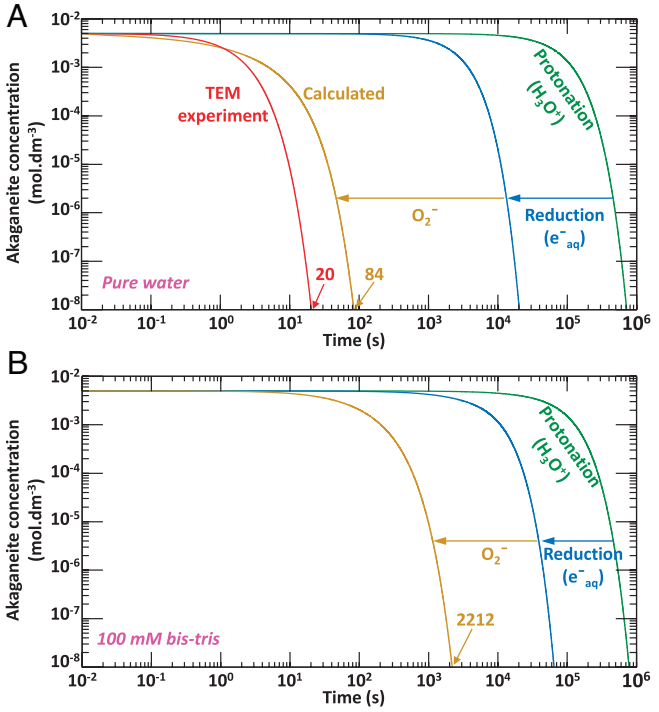

Fig. 3. Simulations of e-beam-induced akaganeite dissolution. (*A*) Predicted time evolution of the concentration of akaganeite in pure, neutral, pH = 7 water irradiated by an electron beam at a dose rate of 0.53 $e^-/Å^2s$ (4.24 × 10^8 Gy/s) corresponding to the dissolution experiments shown in Fig. 1*D*. (*B*) Predicted time evolution of the concentration of akaganeite in the presence of 100 mM of bis-tris irradiated by an electron beam at a dose rate of 0.53 $e^-/Å^2s$ (4.24 × 10^8 Gy/s).

to the dissolution rate. Altogether, the simultaneous contributions of O_2^-, e^-_{aq}, and H_3O^+ are predicted to yield dissolution in 84 s, close to the 20 s measured in the LP-TEM experiments, and three orders of magnitude faster than that observed in the unirradiated acidic batch experiments, close to the observed factor of 186 rate increase. The connection between enhancement of surface chemical reactions by radiolytic products predicted here and the physical mechanism of dissolution, which requires removal of ions from kink sites on the crystal surface, is discussed below.

Manipulation of Dissolution Behavior under Irradiation through Solution Chemistry. Given the quantifiable effect of the e-beam on the dissolution behavior through setting the solution pH and redox conditions, we designed LP-TEM experiments that manipulate these conditions by using pH buffers and varying the dose rate. Bis-tris (BioUltra), which has a pH range of 9.5 to 11.0 (25 °C, 1 M in H_2O), was introduced at concentrations ranging from 20 mM to 100 mM. At 20 mM bis-tris, the measured pH of the akaganeite suspension prior to loading in the liquid cell was 10.60. Using an initial dose rate of 0.67 $e^-/Å^2s$, the in situ LP-TEM observations showed that nanorod dissolution led to thinning of the rods and hollowing out of the rod interiors (Fig. 4*A* and *SI Appendix*, Fig. S5). The latter process clearly suggested the importance of the central nanoporosity in facilitating the dissolution behavior. Furthermore, not surprisingly, given the simulation results above, we observed that the dissolution rate is strongly dependent on the dose rate, as shown in *SI Appendix*, Fig. S6*A*.

To analyze the dissolution of these particles, we first define α as the fraction of the projected cross-sectional area dissolved so that $\alpha = (\pi r_{1,0}r_{2,0} - \pi r_1 r_2)/\pi r_{1,0}r_{2,0} = 1 - (r_1r_2/r_{1,0}r_{2,0}) = 1 - S/S_{Fe,0}$, where S is the projected area of an ellipsoidal nanorod, r_1 and r_2 are the short and long radii, respectively (i.e., W/2 and L/2) and the subscript "0" refers to the value at t = 0. Assuming a constant dissolution rate along each radius then gives $S/S_{Fe,0} = (1 - Kt)^2$ or, alternatively, $1 - (r_1r_2/r_{1,0}r_{2,0})^{1/2} = Kt$, or alternatively, $1 - (1 - \alpha)^{1/2} = Kt$, which reproduces what is known as the geometric contraction model (37, 41), where α is the fraction of the cylinder dissolved and K is the dissolution rate constant, for the case where the cylinder is replaced by an ellipsoid. For these analyses, measuring the evolution of the projected area of the nanorods is sufficient to resolve the various mechanisms such as end-to-end or side-to-side dissolution without requiring additional assumptions, since the TEM images are 2D projections of ellipsoidal particles.

The analysis shows that, for 20 mM bis-tris, when the electron dose rate increases from 0.13 $e/Å^2s$ to 0.78 $e/Å^2s$ and 6.12 $e/Å^2s$ (Movie S3), the order of the dissolution rate constant increases gradually from 10^{-5} to 10^{-2}, yielding increases of about 260 to 2,800 times, respectively (Fig. 4*C*). Notably, the dissolution rate was found to vary linearly with the dose rate (*SI Appendix*, Fig. S7), reinforcing the importance of the steady-state radical concentrations in solution. However, in contrast to the behavior of the nanorods in pure water, their length did not change significantly. This behavior is clearly consistent with the premise that dissolution along the [010] direction is mainly proton promoted, and should thus be inhibited by the presence of bis-tris buffer acting as a sink for radiolytically generated acidity. Moreover, we found that by increasing the bis-tris concentration to 100 mM that nanorod dissolution was completely inhibited; no noticeable change in dimensions could be detected regardless of the dose rate applied, even at a high electron dose rate of 562 $e/Å^2s$ (Fig. 4 *B* and *D* and *SI Appendix*, Fig. S8). This suggests a role for bis-tris that goes beyond simple pH maintenance, such as influencing the steady-state concentration of other radiolytic species.

It is worthwhile to point out that the surface roughness of akaganeite nanorods will influence the estimated surface area, particularly when the calculated surface area is based on the particle's geometry, rather than profilometry measurements on every face. However, the model we use normalizes the surface area to that of the initial rod surface area—i.e., $S/S_{Fe,0}$. (In effect, S and $S_{Fe,0}$ are each products of the area determined from particle geometry and the average surface roughness.) Thus, the effects of roughness are minimized as long as the roughness is of similar magnitude over time. To the extent that it is not, there will be errors in the rate constant K, because the implication of varying surface roughness is that the number of active sites for dissolution is varying. This would immediately lead to a nonlinear dependence of dissolution rate on time—either continuously increasing if surfaces are roughening, or continuously decreasing if roughness is being eliminated. We see neither, so we conclude that roughness is not evolving significantly with time. That is, whatever change in roughness there is small compared to the change in surface area determined from geometry alone. Although the effect of roughness does not impact our conclusions concerning the rate constant or the impact of pH, buffers, or the electron beam on that constant, we have to note that the roughness can influence the surface sites, whose amount can strongly affect the dissolution rate. Generally, the dissolution rate is given by the net difference between the on and off rates of ions at all potential surface sites. Presumably, as in growth, dissolution is overwhelmingly dominated by detachment from sites with the fewest number of nearest neighbors—i.e., the so-called kink sites. It is hard to see how the electron beam could make ion or surface desolvation harder as an input of energy or generation of radicals should work in the opposite fashion. That leaves us with easier removal of ions from surface sites, step sites, and/or kink sites. As all are dependent on disrupting bonds in the solid, the conclusion we come to is that the increased rate of dissolution with increasing

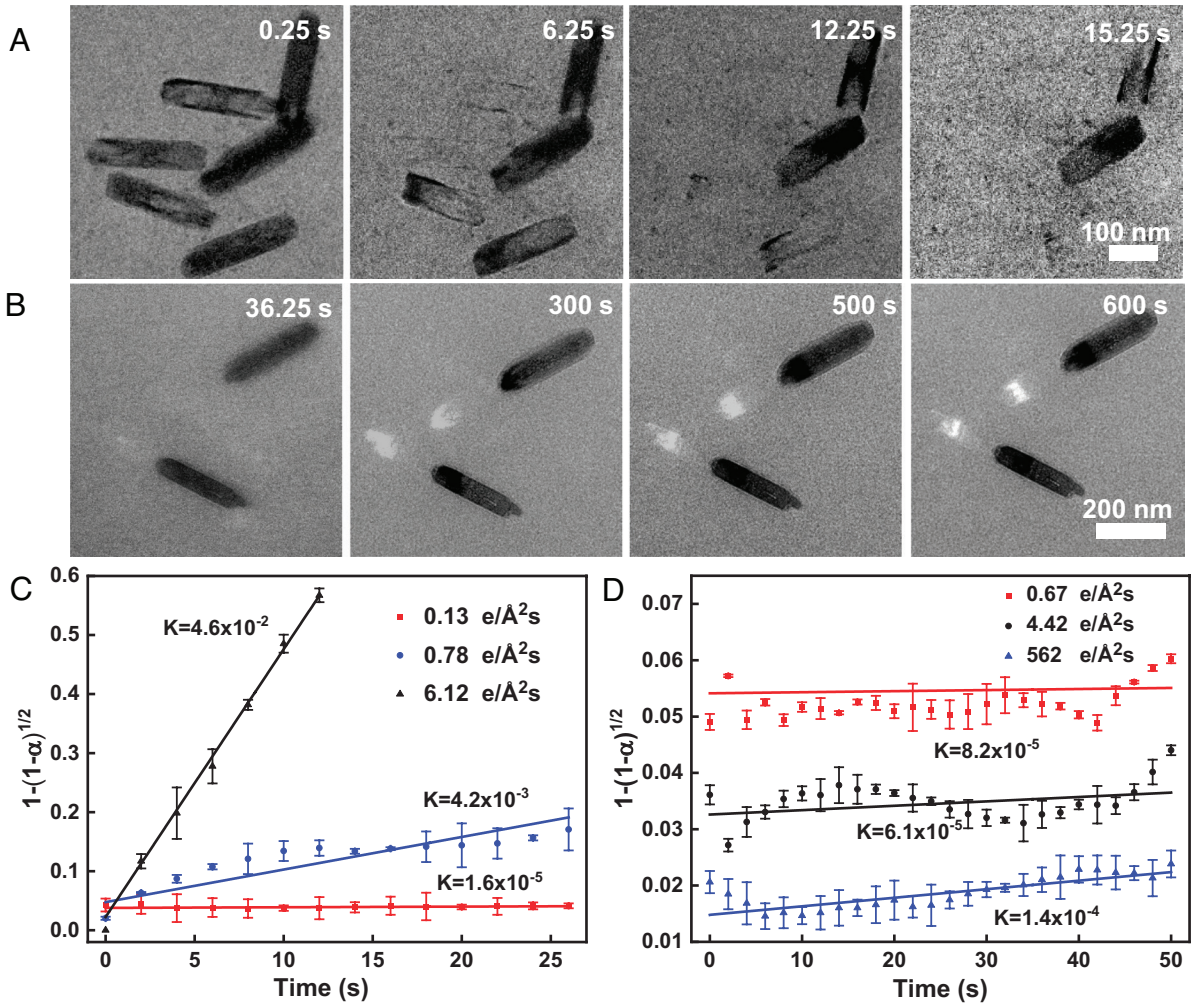

Fig. 4. The effects of bis-tris concentration and electron dose rate on dissolution. (*A* and *B*) Time evolution of akaganeite during dissolution in the presence of (*A*) 20 mM bis-tris at a dose rate of 6.12 e/Å^{2}s and (*B*) 100 mM bis-tris at a dose rate of 4.42 e/Å^{2}s. (*C* and *D*) Dissolution rate at each dose rate in the presence of (*C*) 20 mM bis-tris and (*D*) 100 mM bis-tris plotted as $1 - (1 - \alpha)^{1/2}$ versus time according to the shrinking cylinder model (see text for details). K, obtained from the linear data fitting, is the dissolution rate constant, expressed in s^{-1}. Note: For both in situ experiments, we measured the length and width of more than six nanorods at each time point and then plotted the average value with SD error bars.

electron dose rate reflects an increase in the number density of kink sites due to enhanced rate of bond breaking. This is precisely the conclusion that comes from simulations, which relate that bond breaking to the concentration of radicals through the equilibrium constants for the relevant reactions. Since the concentration of radicals scales with the dose rate at steady state, the rate of removal of ions from the surface sites and, thus, the steady-state dissolution rate do as well (more details in *SI Appendix*, Note 1).

To understand this system more quantitatively, we adapted our radiolytic kinetic model to account for additional scavenging reactions of bis-tris with radiolytic species (42) such as e^-_{aq} and OH• (*SI Appendix*, Table S5). At 100 mM of bis-tris and equivalent dose rates, the concentrations of e^-_{aq} and OH• radicals are predicted to be slightly reduced compared to their concentrations in pure water (*SI Appendix*, Table S6). However, the concentration of O_2^- is predicted to be decreased by three orders of magnitude. Because e^-_{aq} and O_2^- are major beam-induced Fe(III) reductants in our system, their scavenging by bis-tris is predicted to significantly inhibit dissolution so that an additional 2,000 s is needed to dissolve the akaganeite nanorods (Fig. 3*B*). Such a prediction agrees rather well with the observation that akageneite persists in 100 mM Bis-tris beyond 600 s under e-beam irradiation.

Given the evidence for tunability in the dissolution morphology, we explored other adjustments to solution chemistry that conceptually could promote dissolution along [001]/[100] by inhibiting dissolution along the [010] direction. In an LP-TEM experiment, we explored manipulation of the background Cl^- concentration using NaCl addition, while maintaining the protective effect of bis-tris at 100 mM. The reasoning behind increasing the Cl^- activity was twofold. First, the dissolution rate of the nanorods could increase through formation of Fe–Cl surface complexes that can facilitate the rupture of Fe–O bonds (43) and likewise increase the amount of iron that can be solubilized into solution. Second, given the importance of small concentrations of incorporated Cl^- ions for stabilizing the 2 × 2 tunnel structure of akaganeite (44), at [010] nanorod tip surfaces where these tunnels are exposed, the increase in Cl^- activity could selectively decrease the tendency for these surfaces to preferentially dissolve. LP-TEM experiments entailing NaCl added at 50 mM performed across a range of dose rates show, consistent with our hypothesis, that the inhibitory effect of 100 mM bis-tris is indeed overcome, leading to selective enhancement of dissolution along the [001]/[100] directions in the middle portion of the nanorods with no detectable change in nanorod ends (Fig. 5*A* and Movie S4). The extent of dissolution was substantial, in clear contrast to the case without Cl^- ions (Fig. 4*B*), yielding particles completely bisected by dissolution through the middle. Undoubtedly, this was assisted by the nanoporosity in the central regions. Plots of normalized

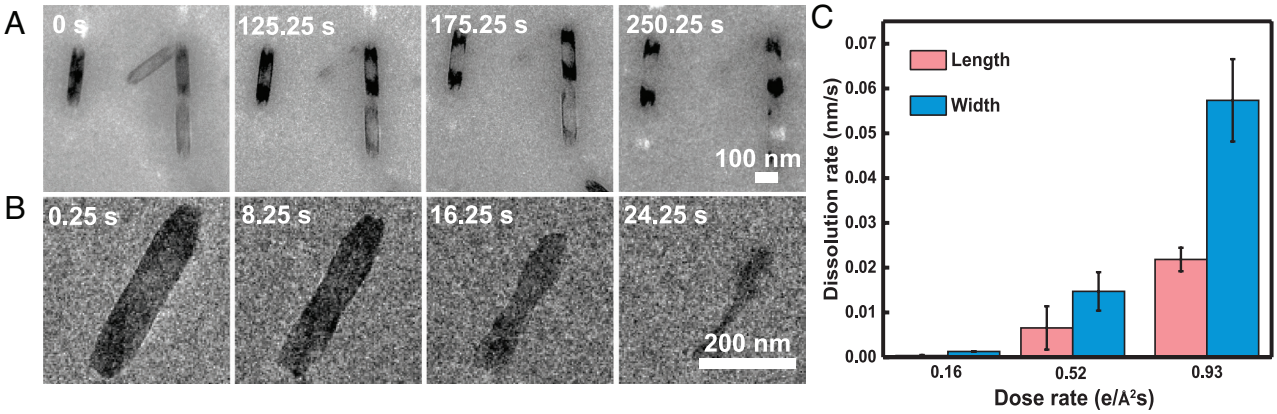

Fig. 5. Time evolution of akaganeite dissolution observed by LPTEM in the presence of (*A*) a mixture of 100 mM bis-tris and 50 mM NaCl at a dose rate of 1.47 e/Å^{2}s. (*B*) 20 mM tris-HCl at a dose rate of 0.86 e/Å^{2}s. (*C*) Comparison of the measured dissolution rate of akaganeite along the width and length in 20 mM tris-HCl at each electron dose rate. Note: We calculated the dissolution rate of each akaganeite nanorod (more than 6) along the width and length and then plotted the average value with SD error bars.

area versus time at dose rates of both 1.47 e/Å^{2}s and 12.4 e/Å^{2}s (*SI Appendix*, Figs. S9 and S10) show, again, that the dissolution rate is highly dependent on the dose rate. More importantly, the collective findings demonstrate the ability to gain control over the dissolution behavior with selective adjustments in solution chemistry given the knowledge of the dissolution mechanism.

As a final test, we returned to experiments in NaCl-free buffer solution, but this time replaced bis-tris with 20 mM tris-HCl buffer which, while maintaining a pH range of 7 to 9, can release Cl^- ions into solution. Thus, with this adjustment, we expected qualitatively similar dissolution behavior compared to added NaCl experiments. Indeed, as shown in Fig. 5*B* (Movie S5), again the akaganeite nanorods tended to dissolve preferentially in the middle relative to the nanorod tips, in this case developing a dumbbell shape during dissolution (see time sequence LP-TEM images in *SI Appendix*, Fig. S11). These experiments provided the clearest evidence yet for the governing influence of the central nanoporosity on the dissolution behavior. Quantitative analysis of the directional dissolution rate shows that tris-HCl drives faster dissolution of the nanorods along [001]/[100] directions relative to that along [010] by a factor of ~2 (Fig. 5*C*), regardless of the dose rate. That dissolution in either direction was again linearly dependent on dose rate is shown in *SI Appendix*, Figs. S12 and S13. In both sets of experiments with Cl-containing additives, these anions appear to play a key role in stabilizing the structural tunnels exposed at the (010) facets of the nanorod tips while simultaneously destabilizing the nanorod structure along [001]/[100] directions.

Collectively, given mechanistic knowledge about the roles of beam-induced radiolysis, acidity, and reductive dissolution on various facets of the akaganeite nanorods, these pH buffer and dose rate experiments demonstrate the ability to gain intentional control over both the overall dissolution rate and the dissolution behavior, under irradiation. We furthermore discovered that although our nanorods contained substantial nanoporous defects, dissolution at these locations could be selectively inhibited or activated by solution chemistry adjustments. For a given dose rate of 0.53 e/Å^{2}s, dissolution rates from various LP-TEM experiments are summarized in Table 1, and associated dissolution morphologies are illustrated in Fig. 6.

Table 1. Dissolution rate constants along the length, width, and areas of akaganeite nanorods for different buffers at a dose rate of 0.53 e/Å^{2}s

Systems	K_L (s^{-1})	K_W(s^{-1})	K_{Area}(s^{-1})
Pure water	0.050	0.030	—
Bis-tris (low)	—	—	0.0027
Tris-HCl	0.010	0.022	0.019

Conclusion

A combination of LP-TEM, solution chemistry, and radiolytic speciation simulations informed by knowledge of various possible dissolution mechanisms was used successfully to both manipulate the dissolution behavior and rate of akageneite nanorods and quantitatively account for e-beam-induced radiolytic speciation. Our findings show that beam-induced radiolysis of the aqueous solution contributes to two main processes: i) acid-promoted [010] dissolution, and ii) reduction of lattice Fe(III) to soluble Fe(II), which drives [001]/[100] dissolution. The addition of pH buffers to offset the acidity selectively decreases and can even eliminate dissolution along [010]. While a similar effect arises from the addition of chloride ions, this also enhances dissolution along [001]/[100] by complexation. Simulations of chemical equilibria and dissolution indicate that organic buffers such as bis-tris can selectively reduce the availability of superoxides and aqueous electrons, thereby suppressing dissolution rates. This work provides strong evidence that LP-TEM can be used to exploit anisotropies in reductive and acidic dissolution mechanisms for Fe(III)-(oxyhydr)oxides to arrive at tuned morphologies, providing a unique platform for testing hypotheses for dissolution mechanisms presumed from macroscopic batch studies. Considering certain conceptual similarities between radiolysis and photolysis, the present findings may also provide clues about the fundamental processes controlling the dissolution rate and morphologies of iron oxides and oxyhydroxides in the photic zone of natural aquatic systems. More importantly, the cycling of iron between its +2 and +3 oxidation states is the centerpiece of the iron cycle, a key component of which is the reductive dissolution of ferric oxyhydroxide minerals. The fact that our results show that both the absolute and relative dissolution rates along different facet directions (i.e., length versus width) change dramatically when conditions evolve from acidic to reductive to buffered, demonstrates the impact of local environmental conditions on iron oxide dissolution rates and mechanisms. These insights also suggest a possible route to reconstruction of those conditions during deposition or diagenesis or subsequent alteration via analysis of specific crystallite morphologies. By enhancing our understanding of interfacial processes

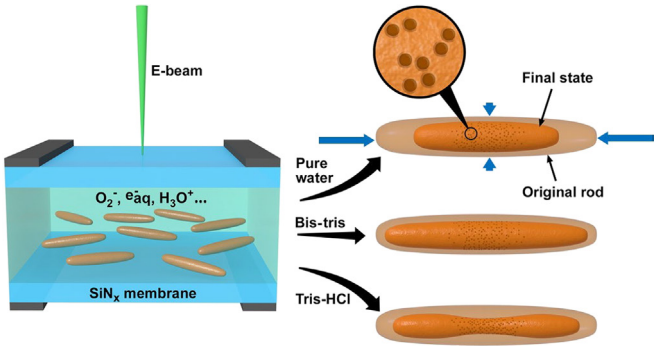

Fig. 6. Conceptual models of the various dissolution morphologies assessed by our various LP-TEM experiments.

governing iron oxide dissolution, the findings provide a unique basis for interpreting geochemical and biogeochemical signatures governing iron redox cycling across a diversity of crustal and aquatic environments.

Methods

Akaganeite Synthesis. The akaganeite nonorods were synthesized via a hydrothermal method. Briefly, $FeCl_3 \cdot 6H_2O$ was dissolved into DI water to form a 0.5 M solution, and then 80 mL solution was transferred into a 125-mL Teflon liner. The liner was sealed into a Parr steel vessel and then was heated in an electric oven at 80 °C for 3 d. After cooling the Parr vessel to room temperature, the final product was collected by centrifugation, washed with DI water three times, and dried at 80 °C overnight.

STEM HAADF Imaging and Chemical Composition Analysis. STEM was used to probe the defect distribution on the surface of the akaganeite nanorod in prepared samples. The procedure was performed with an FEI Titan 80-300 microscope operated at 300 kV. The instrument is equipped with a CEOS GmbH double-hexapole aberration corrector for the probe-forming lens, which allows for imaging with 0.1 nm resolution in STEM. The tilt angles ranges from −66° to +66° in increments of 2°. The images were acquired with a HAADF detector with inner collection angle set to 52 mrad. The chemical composition of akaganeite nanorods was analyzed by STEM energy-dispersive X-ray spectroscopy (EDS) mapping with an Oxford EDS detector (Oxford Instruments Analytical Ltd.) and XPS.

Liquid-Phase TEM (LP-TEM). All LP-TEM experiments were performed in a 200-kV field emission electron microscope (FEI Tecnai F20) using the liquid-cell holder (Hummingbird Scientific, USA) based on microfabricated silicon chips. Two square silicon chips containing silicon nitride membranes were separated with 100 nm gold spacers deposited on the two strips. Prior to loading the solution, the membranes were oxygen plasma cleaned for 1 min to remove organic contaminants and render the surfaces hydrophilic. The akaganeite suspension was deposited between the two membranes in 0.5 μL droplets placed onto the bottom side of the membrane followed by capping with an upper chip. The liquid cell was mounted and sealed on the holder using O-rings. The assembled liquid-cell stage was vacuum tested in a Pfeiffer vacuum chamber. The images were recorded using a FEI Eagle charge-coupled device camera. Continuous movies were captured using a freeware screen grabber (VirtualDub).

Deterministic Simulations. The interaction of ionizing radiations, such as high-energy electrons, with water is well understood both experimentally and theoretically (28, 45, 46). One microsecond after the initial water-ionizing radiation interaction, the longest-lived transient species generated by water radiolysis, named primary yields, can be summarized by:

$$H_2O \rightarrow e^-_{aq}, OH\cdot, H\cdot, HO_2\cdot, H^+, OH^-, H_2O_2, H_2 \qquad [1]$$

The amount of primary yields produced per 100 eV of energy loss, commonly referred as the *G*-values, depends on several conditions such as temperature, radiation type and energy, and solution composition. For high-energy electrons, as generated by the 200 kV electron beam used in this work, the *G*-values used for the generation of primary yields were obtained from Hill and Smith (47) and are given in *SI Appendix*, Table S2. The electron beam radiation dose rate for water was calculated by the formula provided by Schneider et al. (28) and the calculation details for the specific experimental conditions of this study are given in *SI Appendix*, Table S1.

In order to follow the temporal chemical evolution of the system under electron beam irradiation, deterministic simulations were performed using the Chemsimul program (48), which translates a set of chemical reactions into a system of ordinary differential equations and solve the coupled kinetic equations. To simulate water radiolysis, a set of 65 chemical reactions (46) was used. Assuming that an initial concentration of 5 mM akaganeite (β–FeOOH) was present in the system, and that dissolution occurs, 88 additional chemical reactions (49) describing the interaction of iron with water radiolysis species were added to complete the water radiolysis model. The complete list of chemical reactions and rate constants used can be found in *SI Appendix*, Tables S3 and S6. To describe akaganeite dissolution, an interface model using diffusion range limitations of radiolytic species was developed, as shown in *SI Appendix*, Table S7 and Fig. S14. In this model, the rate constants traditionally used for homogeneous bulk chemistry were modified to describe interface systems. Further details on the interface model are given in *SI Appendix*. The interface model was used to quantify the contributions of protonation, reduction, radiolytic products, and bis-tris buffer in the dissolution of akaganeite. The effect of pH on protonation and reduction dissolution rates of akaganeite was determined based on two well-known minerals, as shown in *SI Appendix*, Table S9 and Fig. S15.

Data, Materials, and Software Availability. All study data are included in the article and/or *SI Appendix*.

ACKNOWLEDGMENTS. We thank Mark H. Engelhard for X-ray photoelectron spectroscopy measurement and Mark Bowden for X-ray diffraction (XRD) data analysis. We also thank X. R. Liang for helping with drawing Scheme 1. This material is based upon work supported by the U.S. Department of Energy (DOE), Office of Science, Office of Basic Energy Sciences, Chemical Sciences, Geosciences, and Biosciences Division through its Geosciences program at Pacific Northwest National Laboratory (PNNL) (FWP 56674). The scanning electron microscopy, XRD, and 3D tomography scanning transmission electron microscopy were performed under user proposal 51382 at the Environmental Molecular Science Laboratory, a DOE Office of Science User Facility sponsored by the Office of Biological and Environmental Research and located at PNNL.

Author affiliations: [a]Physical and Computational Sciences Directorate, Pacific Northwest National Laboratory, Richland, WA 99352; and [b]Department of Materials Science and Engineering, University of Washington, Seattle, WA 98195

Author contributions: L.L., X.Z., K.M.R., and J.J.D.Y. designed research; L.L. and M.S. performed research; L.K. and S.X. contributed new reagents/analytic tools; L.L., X.Z., E.N., J.J.D.Y., and B.J. analyzed data; and L.L., X.Z., K.M.R., and J.J.D.Y. wrote the paper.

1. G. Rubasinghege, R. W. Lentz, M. M. Scherer, V. H. Grassian, Simulated atmospheric processing of iron oxyhydroxide minerals at low pH: Roles of particle size and acid anion in iron dissolution. *Proc. Natl. Acad. Sci. U.S.A.* **107**, 6628–6633 (2010).
2. K. Klyukin, K. M. Rosso, V. Alexandrov, Iron Dissolution from goethite (α-FeOOH) surfaces in water by Ab Initio enhanced free-energysimulations. *J. Phys. Chem. C* **122**, 16086–16091 (2018).
3. S. D. Taylor *et al.*, Visualizing the iron atom exchange front in the Fe(II)-catalyzed recrystallization of goethite by atom probe tomography. *Proc. Natl. Acad. Sci. U.S.A.* **116**, 2866–2874 (2019).
4. A. J. Frierdich *et al.*, Iron atom exchange between hematite and aqueous Fe(II). *Environ. Sci. Technol.* **49**, 8479–8486 (2015).
5. M. Zong *et al.*, Synthesis of 2D hexagonal hematite nanosheets and the crystal growth mechanism. *Inorg. Chem.* **58**, 16727–16735 (2019).
6. L. Machala, J. Tuček, R. Zbořil, Polymorphous transformations of nanometric iron(III) oxide: A review. *Chem. Mater.* **23**, 3255–3272 (2011).
7. C. Frandsen *et al.*, Aggregation-induced growth and transformation of β-FeOOH nanorods to micron-sized α-Fe_2O_3 spindles. *CrystEngComm* **16**, 1451–1458 (2014).

8. V. M. Yuwono, N. D. Burrows, J. A. Soltis, R. L. Penn, Oriented aggregation: Formation and transformation of mesocrystal intermediates revealed. *J. Am. Chem. Soc.* **132**, 2163–2165 (2010).
9. J. F. Banfield, S. A. Welch, H. Zhang, T. T. Ebert, R. L. Penn, Aggregation-based crystal growth and microstructure development in natural iron oxyhydroxide biomineralization products. *Science* **289**, 751–754 (2000).
10. R. M. Cornell, R. Giovanoli, Transformation of akaganéite into goethite and hematite in alkaline media. *Clay Clay Miner.* **38**, 469–476 (1990).
11. A. J. Anschutz, R. L. Penn, Reduction of crystalline iron(III) oxyhydroxides using hydroquinone: Influence of phase and particle size. *Geochem. Trans.* **6**, 60 (2005).
12. J. J. Erbs, B. Gilbert, R. L. Penn, Influence of size on reductive dissolution of six-line ferrihydrite. *J. Phys. Chem. C* **112**, 12127–12133 (2008).
13. P. S. Sidhu, R. J. Gilkes, R. M. Cornell, A. M. Posner, J. P. Quirk, Dissolution of iron oxides and oxyhydroxides in hydrochloric and perchloric acids. *Clay Clay Miner.* **29**, 269–276 (1981).
14. J. G. Wiederhold *et al.*, Iron isotope fractionation during proton-promoted, ligand-controlled, and reductive dissolution of goethite. *Environ. Sci. Technol.* **40**, 3787–3793 (2006).
15. S. G. Benner, C. M. Hansel, B. W. Wielinga, T. M. Barber, S. Fendorf, Reductive dissolution and biomineralization of iron hydroxide under dynamic flow conditions. *Environ. Sci. Technol.* **36**, 1705–1711 (2002).
16. J. M. Smolen, M. A. McLaughlin, M. J. McNevin, A. Haberle, S. Swantek, Reductive dissolution of goethite and the subsequent transformation of 4-cyanonitrobenzene: Role of ascorbic acid and pH. *Aquat. Sci.* **65**, 308–315 (2003).
17. X. Huang *et al.*, Photo-production of reactive oxygen species and degradation of dissolved organic matter by hematite nanoplates functionalized by adsorbed oxalate. *Environ. Sci. Nano* **7**, 2278–2292 (2020).
18. W. Feng, D. Nansheng, Photochemistry of hydrolytic iron (III) species and photoinduced degradation of organic compounds. A minireview. *Chemosphere* **41**, 1137–1147 (2000).
19. I. Štyriaková *et al.*, Metal leaching and reductive dissolution of iron from contaminated soil and sediment samples by indigenous bacteria and bacillus isolates. *Soil Sediment Contam.* **25**, 519–535 (2016).
20. Z. Wang, H. Fu, L. Zhang, W. Song, J. Chen, Ligand-promoted photoreductive dissolution of goethite by atmospheric low-molecular dicarboxylates. *J. Phys. Chem. A* **121**, 1647–1656 (2017).
21. R. M. Cornell, U. Schwertmann, *The Iron Oxides* (2003), Wiley, pp. 297–344.
22. S. Kerisit, K. M. Rosso, Computer simulation of electron transfer at hematite surfaces. *Geochim. Cosmochim. Acta* **70**, 1888–1903 (2006).
23. P. Zarzycki, S. Kerisit, K. M. Rosso, Molecular dynamics study of Fe(II) Adsorption, electron exchange, and mobility at goethite (α-FeOOH) surfaces. *J. Phys. Chem. C* **119**, 3111–3123 (2015).
24. S. W. Poulton, D. E. Canfield, Development of a sequential extraction procedure for iron: Implications for iron partitioning in continentally derived particulates. *Chem. Geol.* **214**, 209–221 (2005).
25. J. G. Reynolds, The apparent solubility of aluminum (III) in Hanford high-level waste. *J. Environ. Sci. Health A Tox. Hazard. Subst. Environ. Eng.* **47**, 2213–2218 (2012).
26. Q. Chen *et al.*, Interaction potentials of anisotropic nanocrystals from the trajectory sampling of particle motion using in situ liquid phase transmission electron microscopy. *ACS Cent. Sci.* **1**, 33–39 (2015).
27. F. Yan *et al.*, Controlled synthesis of highly-branched plasmonic gold nanoparticles through peptoid engineering. *Nat. Commun.* **9**, 2327 (2018).
28. N. M. Schneider *et al.*, Electron-Water interactions and implications for liquid cell electron microscopy. *J. Phys. Chem. C* **118**, 22373–22382 (2014).
29. T. J. Woehl, P. Abellan, Defining the radiation chemistry during liquid cell electron microscopy to enable visualization of nanomaterial growth and degradation dynamics. *J. Microsc.* **265**, 135–147 (2017).
30. L. Liu *et al.*, Connecting energetics to dynamics in particle growth by oriented attachment using real-time observations. *Nat. Commun.* **11**, 1045 (2020).
31. V. Alexandrov, K. M. Rosso, Electron transport in pure and substituted iron oxyhydroxides by small-polaron migration. *J. Chem. Phys.* **140**, 234701 (2014).
32. P. Vennéguès, F. Tendille, P. De Mierry, Study of defect management in the growth of semipolar (11–22) GaN on patterned sapphire. *J. Phys. D Appl. Phys.* **48**, 325103 (2015).
33. M. Khafizov *et al.*, Combining mesoscale thermal transport and x-ray diffraction measurements to characterize early-stage evolution of irradiation-induced defects in ceramics. *Acta Mater.* **193**, 61–70 (2020).
34. R. M. Handler *et al.*, Fe(II)-catalyzed recrystallization of goethite revisited. *Environ. Sci. Technol.* **48**, 11302–11311 (2014).
35. P. Joshi, C. A. Gorski, ANisotropic morphological changes in goethite during Fe2+-catalyzed recrystallization. *Environ. Sci. Technol.* **50**, 7315–7324 (2016).
36. S. V. Yanina, K. M. Rosso, Linked reactivity at mineral-water interfaces through bulk crystal conduction. *Science* **320**, 218–222 (2008).
37. L. Fedunik-Hofman, A. Bayon, S. W. Donne, Kinetics of solid-gas reactions and their application to carbonate looping systems. *Energies* **12**, 2981 (2019).
38. X. Huang *et al.*, Facet-specific photocatalytic degradation of organics by heterogeneous fenton chemistry on hematite nanoparticles. *Environ. Sci. Technol.* **53**, 10197–10207 (2019).
39. M. Wolszczak, J. Gajda, Iron release from ferritin induced by light and ionizing radiation. *Res. Chem. Intermed.* **36**, 549–563 (2010).
40. U. Schwertmann, Solubility and dissolution of iron oxides. *Plant Soil* **130**, 1–25 (1991).
41. T. C. Alex, R. Kumar, S. K. Roy, S. P. Mehrotra, Leaching behaviour of high surface area synthetic boehmite in NaOH solution. *Hydrometallurgy* **137**, 23–32 (2013).
42. J. A. Manion *et al.*, *National Institute of Standards and Technology*, Gaithersburg, Maryland, 20899-8320.
43. R. M. Cornell, A. M. Posner, J. P. Quirk, Kinetics and mechanisms of the acid dissolution of goethite (α-FeOOH). *J. Inorg. Nucl. Chem.* **38**, 563–567 (1976).
44. R. M. Cornell, R. Giovanoli, Acid dissolution of akaganiéite and lepidocrocite: The effect on crystal morphology. *Clay Miner.* **36**, 385–390 (1988).
45. S. Le Caer, Water radiolysis: Influence of oxide surfaces on H_2 production under ionizing radiation. *Water* **3**, 235–253 (2011).
46. B. Pastina, J. A. LaVerne, Effect of molecular hydrogen on hydrogen peroxide in water radiolysis. *J. Phys. Chem. A* **105**, 9316–9322 (2001).
47. M. A. Hill, F. A. Smith, Calculation of initial and primary yields in the radiolysis of water. *Radiat. Phys. Chem.* **43**, 265–280 (1994).
48. P. Kirkegaard, E. Bjergbakke, J. V. Olsen, *Chemsimul: A Chemical Kinetics Software Package* (Danmarks Tekniske Universitet, 2008).
49. P. Bouniol, The influence of iron on water radiolysis in cement-based materials. *J. Nucl. Mater.* **403**, 167–183 (2010).